

See discussions, stats, and author profiles for this publication at: <https://www.researchgate.net/publication/231646976>

# Metals (Ni, Fe)–Incorporated Titanate Nanotubes Induced Destabilization of LiBH<sub>4</sub>

ARTICLE *in* THE JOURNAL OF PHYSICAL CHEMISTRY C · APRIL 2011

Impact Factor: 4.77 · DOI: 10.1021/jp111752w

CITATIONS

16

READS

14

10 AUTHORS, INCLUDING:



Fen Li

Shanghai Jiao Tong University

53 PUBLICATIONS 311 CITATIONS

SEE PROFILE



Shu-Sheng Liu

Kyushu University

26 PUBLICATIONS 333 CITATIONS

SEE PROFILE



Jian Zhang

Shandong University

168 PUBLICATIONS 3,632 CITATIONS

SEE PROFILE



M. Zhu

South China University of Technology

235 PUBLICATIONS 2,722 CITATIONS

SEE PROFILE

# Metals (Ni, Fe)-Incorporated Titanate Nanotubes Induced Destabilization of LiBH<sub>4</sub>

Xiaoliang Si,<sup>†,‡</sup> Fen Li,<sup>†</sup> Lixian Sun,<sup>†,\*</sup> Fen Xu,<sup>§,\*</sup> Shusheng Liu,<sup>†</sup> Jian Zhang,<sup>†</sup> Min Zhu,<sup>⊥</sup> Liu-Zhang Ouyang,<sup>⊥</sup> Dalin Sun,<sup>||</sup> and Ying-Liang Liu<sup>\*,#</sup>

<sup>†</sup>Materials and Thermochemistry Laboratory, Dalian Institute of Chemical Physics, Chinese Academy of Sciences, Dalian 116023, China

<sup>‡</sup>Graduate School of Chinese Academy of Sciences, Beijing 100049, China

<sup>§</sup>Faculty of Chemistry and Chemical Engineering, Liaoning Normal University, Dalian 116029, China

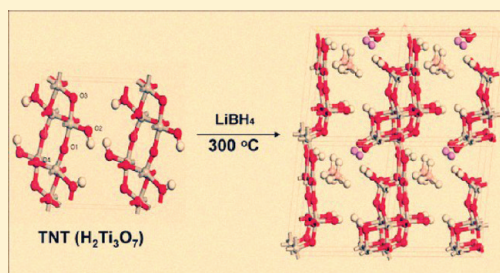
<sup>⊥</sup>School of Materials Science and Engineering, South China University of Technology, Guangzhou 510640, China

<sup>||</sup>Department of Material Science, Fudan University, 220 Handan Road, Shanghai 200433, China

<sup>#</sup>Jinan University, Department of Chemistry, Guangzhou 510632, Guangdong, China

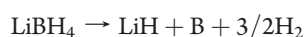
**S** Supporting Information

**ABSTRACT:** Metals (Ni, Fe)-incorporated titanate nanotubes (M–TNT, M = Ni, Fe) with H<sub>2</sub>Ti<sub>3</sub>O<sub>7</sub> structure were synthesized to destabilize the LiBH<sub>4</sub> for hydrogen storage. The onset temperature of dehydrogenation was reduced to 100 °C for LiBH<sub>4</sub> and M–TNT composite, which could release 4.5 wt % hydrogen at 120 °C and 11 wt % hydrogen at 260 °C from LiBH<sub>4</sub>. Our experiment results indicate that ball-milled LiBH<sub>4</sub>/Ni–TNT sample has a better dehydrogenation performance than ball-milled LiBH<sub>4</sub>/Ni/H<sub>2</sub>Ti<sub>3</sub>O<sub>7</sub> nanotube and ball-milled LiBH<sub>4</sub>/NiO/H<sub>2</sub>Ti<sub>3</sub>O<sub>7</sub> nanotube samples. Furthermore, one finds that the release of poisoning species like BH<sub>3</sub> and B<sub>2</sub>H<sub>6</sub> could be inhibited by nanotube with H<sub>2</sub>Ti<sub>3</sub>O<sub>7</sub> structure rather than that with anatase structure. The interactions between LiBH<sub>4</sub> and different structure nanotubes are investigated by the first-principle calculation in the present work.



## INTRODUCTION

Complex hydrides with high hydrogen content are potential hydrogen storage materials.<sup>1–3</sup> These so-called complex hydrides containing low-atomic-weight metal cations and anions of borohydride (BH<sub>4</sub><sup>–</sup>), alanate (AlH<sub>4</sub><sup>–</sup>), or amide (NH<sub>2</sub><sup>–</sup>) have both high volumetric and gravimetric capacities for hydrogen.<sup>4–7</sup> Lithium borohydride (LiBH<sub>4</sub>, also named lithium tetrahydroborate) has recently attracted great interest owing to its large theoretical hydrogen capacity (18.5 wt %) and efficient capacity (13.8 wt %).<sup>8</sup> Unfortunately, the practical application of such a hydride in mobile fuel cell system is limited by tough issues of both thermodynamics and kinetics. It was observed that, LiBH<sub>4</sub> melts at approximately 280 °C, the dehydrogenation reaction starts slowly from the liquid state (above 400 °C) to generate a material mixture of boron and lithium hydride as the following equation:<sup>9</sup>



The complete release of the whole hydrogen content of LiBH<sub>4</sub> remains difficult, due to the high decomposition temperature (above 600 °C) of LiH. Recently, many efforts are focused on doping additives, for example, metal halides,<sup>10–13</sup> amides,<sup>14</sup> metal hydrides,<sup>15,16</sup> or oxides,<sup>17</sup> to lower the dehydrogenation

temperature. The other attempts to enhance hydrogen release are based on minimizing the LiBH<sub>4</sub> particle size through confinement within mesoporous host materials.<sup>18,19</sup>

Previous results have indicated that after ball milling with MgH<sub>2</sub>,<sup>20,21</sup> the onset dehydrogenation temperature of LiBH<sub>4</sub> was reduced to below 400 °C and LiBH<sub>4</sub> combined with LiNH<sub>2</sub> generated a new borohydride-amide salt whose decomposition temperature was at 250 °C.<sup>22</sup> Züttel and co-workers<sup>8</sup> reported that hydrogen released from a LiBH<sub>4</sub>–SiO<sub>2</sub> mixture (25 wt % LiBH<sub>4</sub> and 75 wt % SiO<sub>2</sub>) started at 200 °C and Yu et al.<sup>23</sup> found that the onset temperature of dehydrogenation of LiBH<sub>4</sub>–TiO<sub>2</sub> particle composites (20 wt % LiBH<sub>4</sub> and 80 wt % TiO<sub>2</sub>) was at 150 °C. Recent study shows that LiBH<sub>4</sub> confined in porous carbonaceous materials, and its temperature of dehydrogenation decreased to 200 °C.<sup>24</sup> Here, we report a dramatic reduction in the hydrogen release temperature of LiBH<sub>4</sub> through destabilization by metal-incorporated titanate nanotubes, and the kinetic of hydrogen release is largely improved compared to pure LiBH<sub>4</sub>. Furthermore, we find for the first time that H<sub>2</sub>Ti<sub>3</sub>O<sub>7</sub> nanotubes incorporated in the LiBH<sub>4</sub> can effectively inhibit the release of

**Received:** December 10, 2010

**Revised:** February 17, 2011

**Published:** April 21, 2011

poisoning species like  $\text{BH}_3$  and  $\text{B}_2\text{H}_6$  from  $\text{LiBH}_4$  composite, while these poisoning species have been observed during the decomposition of  $\text{LiBH}_4$  and anatase titanate nanotube composite without  $\text{H}_2\text{Ti}_3\text{O}_7$  structure. The interactions between  $\text{LiBH}_4$  and different structure nanotubes are investigated by the first-principle calculation in the present work.

## EXPERIMENTAL SECTION

**Materials and Methods.** Titanate nanotubes (denoted as TNT) and metal-incorporated titanate nanotubes (denoted as M-TNT) were synthesized according to reported procedures.<sup>25,26</sup> In a typical synthesis, commercial anatase  $\text{TiO}_2$  powder with BET surface  $11 \text{ m}^2 \text{ g}^{-1}$  and particle size ranging from 100 to 200 nm was added into a 10 M NaOH aqueous solution. After stirring for 12 h, the solution was transferred into a sealed Teflon container. For metal-incorporated titanate nanotubes, some solid  $\text{FeCl}_3$  or  $\text{NiCl}_2$  (molar ratio of  $\text{TiO}_2/\text{FeCl}_3$  or  $\text{NiCl}_2$  was 10:1) was added into the solution with further stirring for another 12 h, then transferred into Teflon container. All Teflon reactors were heated at  $130^\circ\text{C}$  for 72 h. After the hydrothermal treatment, the powder product was first obtained. Then, the anatase structure nanotubes and  $\text{H}_2\text{Ti}_3\text{O}_7$  structure nanotubes can be obtained by washing the above powder products with  $0.05 \text{ mol dm}^{-3}$   $\text{H}_2\text{SO}_4$  and with water, respectively. All nanotubes were heated to  $400^\circ\text{C}$  for 3 h under Ar to remove the water, then stored in an Unilab91200 glovebox (MBraun Co., Germany) filled with purified argon. After calcination,  $\text{H}_2\text{Ti}_3\text{O}_7$  nanotubes also keep  $\text{H}_2\text{Ti}_3\text{O}_7$  phase. Commercial  $\text{LiBH}_4$  (95%, Alfa Aesar) powder was directly used without further purification. Mixtures of  $\text{LiBH}_4$  and nanotubes with weight ratio of 1:3 were ball milled (QM-1SP planetary ball mill) for different amount of time. In each stainless milling pot (100 mL), the ball-to-powder weight ratio was 50:1 and the protection atmosphere was 0.1 MPa of Ar. All handlings of the sample were conducted in glovebox filled with high-purity Ar (99.9999%) and low-density  $\text{H}_2\text{O}$  and  $\text{O}_2$  (both  $<0.1 \text{ ppm}$ ). The mass content of  $\text{LiBH}_4$  for all samples in this article is 25 wt % unless otherwise noted.

**Theoretical Calculation Method.** First-principles calculations were performed using DFT and planewave pseudopotential technique, as implemented in the CASTEP program.<sup>27</sup> We adopted the generalized gradient approximation (GGA) of Perdew–Burke–Ernzerhof (PBE) functional<sup>28</sup> for exchange–correlation interaction and the ultrasoft pseudopotentials<sup>29</sup> for ion–electron interaction. All calculations were done on the one unit cell for both of anatase  $\text{TiO}_2$  (4 formulas, 12 atoms) and  $\text{H}_2\text{Ti}_3\text{O}_7$  (2 formulas, 24 atoms) structure. A cutoff energy of 350 eV was used for the planewave basis. The Brillouin zone was sampled by a  $7 \times 7 \times 3$  k grid and  $3 \times 7 \times 3$  in geometry optimization and molecular dynamics calculation for anatase  $\text{TiO}_2$  and  $\text{H}_2\text{Ti}_3\text{O}_7$ , respectively. From our calculation, the equilibrium lattice constant are  $a = b = 3.80 \text{ \AA}$  and  $c = 9.75 \text{ \AA}$  for anatase  $\text{TiO}_2$ ,  $a = 8.87 \text{ \AA}$ ,  $b = 3.77 \text{ \AA}$ , and  $c = 9.43 \text{ \AA}$  for  $\text{H}_2\text{Ti}_3\text{O}_7$ . The adsorption energy was defined as:

$$E_{\text{ad}} = E[A + B] - E[A] - E[B]$$

where  $E[X]$  means the total energy of the system X.

**Characterizations.** The isothermal dehydrogenation kinetics was measured by a Sievert-type apparatus (Advanced Materials Corporation) at different temperatures. The gaseous compositions from samples decomposition were detected by a coupled TG/MS technique. Thermo-gravimetric analysis (TG) was carried out on a Cahn Thermax 500, and Mass spectra (MS) were performed on a multicomponent online gas analyzer

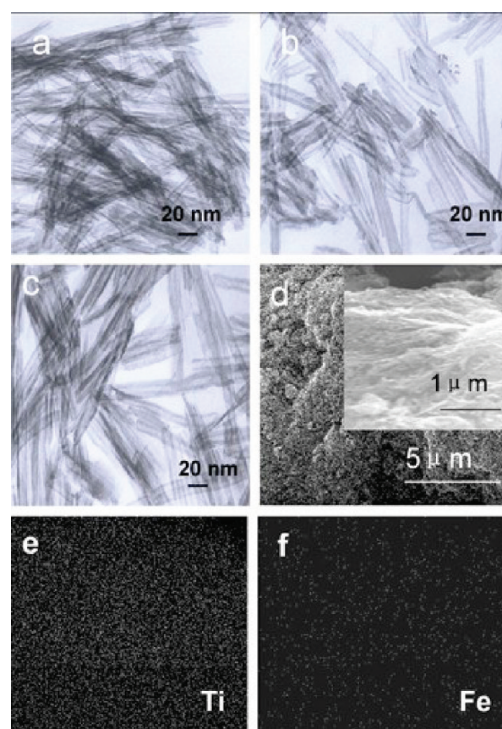


**Figure 1.** Low magnification TEM image of (a) TNT (anatase), (b) Ni-TNT, and (c) Fe-TNT; (d) SEM image of Fe-TNT; (e) the element map of titanium for the image of (d); (f) the element map of iron for the image of (d).

GAM 200. All thermal analyses were measured from room temperature to 873 K at a heating rate of  $5 \text{ K min}^{-1}$  with an argon purge rate of  $50 \text{ mL min}^{-1}$ . X-ray powder diffraction (XRD) was collected on a conventional PANalytical X-ray Diffractometer at 40 kV, 40 mA, with a scan speed of  $5^\circ \text{ min}^{-1}$  and a step size of  $0.02^\circ$  in  $2\theta$ , using  $\text{Cu K}\alpha$  radiation. The SEM photomicrograph of the samples was taken in a JSM-6360LV microscope with Au coating and TEM images were taken using JEM-2000EX. UV–vis spectra were measured with a Cintra 20 (Australian) spectrometer in reflection mode.  $\text{N}_2$  adsorption–desorption measurement was performed on Quantachrome Autosorb-1 at 77 K.

## RESULTS AND DISCUSSION

**Characterization of Nanotubes.** The dimensions, morphology, and chemical composition of the as-prepared nanotubes were examined using the TEM (transmission electron microscopy), SEM (scanning electron microscopy), and EDS (electron dispersive spectrometry). TEM images of the specimen (parts a, b, and c of Figure 1) show an overall view of titanate nanotubes and (Ni, Fe)-incorporated titanate nanotubes, revealing large quantity of tubular materials with narrow size distribution. The outer and inner diameters of the tubular materials are almost uniform around 10 and 3 nm, respectively. The length range is from several tens to several hundreds of nanometers. TEM observations also demonstrated that titanate nanotubes and metal-incorporated titanate nanotubes have similar tubular structures and yields of nanotubes are high. SEM images of Fe-TNT (part d of Figure 1) show that the particles are quite fine and it seems that some wire-like materials compact to form the fine particle. Panels e and f in Figure 1 are the maps for the

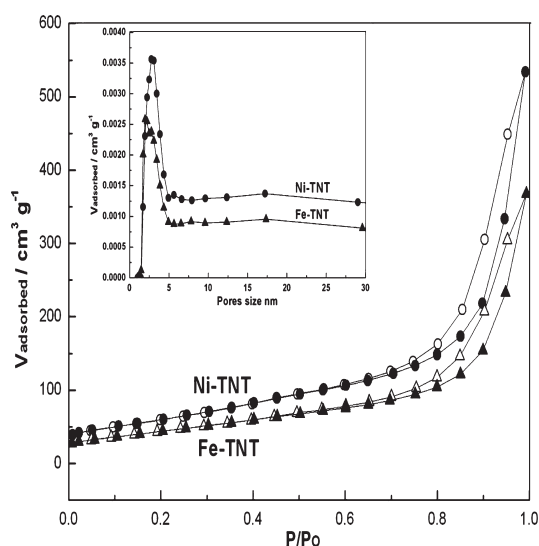


**Figure 2.**  $\text{N}_2$  adsorption (solid) and desorption (dashed) isotherm of Ni-TNT (circles) and Fe-TNT (triangles). The insert shows the pore size distribution.

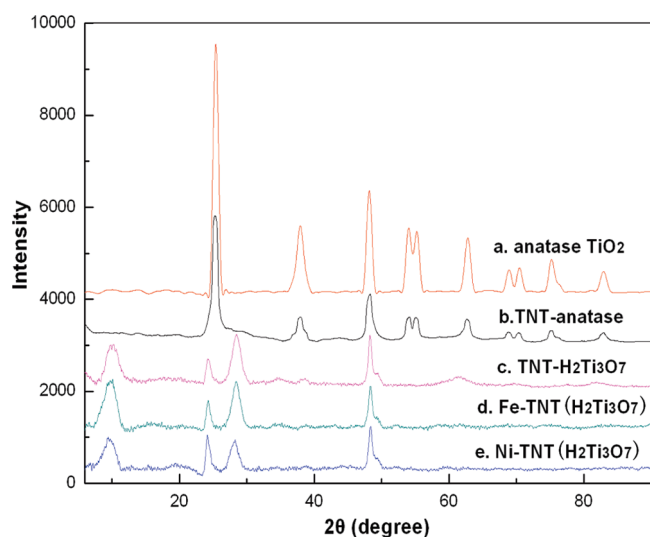


**Figure 3.** XRD patterns of different nanotubes.

elemental distribution of Ti and Fe in the area of part d of Figure 1. The Ti map follows the structure of nanotubes and Fe map is consistent well with Ti map. This suggests that Fe atoms are well dispersed in nanotubes.

$\text{N}_2$  adsorption/desorption analysis (Figure 2) shows that the surface area and pore volume are  $220 \text{ m}^2 \text{ g}^{-1}$  and  $0.83 \text{ cm}^3 \text{ g}^{-1}$  for Ni-TNT,  $162 \text{ m}^2 \text{ g}^{-1}$  and  $0.57 \text{ cm}^3 \text{ g}^{-1}$  for Fe-TNT, respectively. The pore size is around 3 nm, this is consistent well with TEM observations. UV-vis absorption spectra (Figure S1 of the Supporting Information) show that the metal-incorporated nanotube has an improved photon absorption efficiency in the visible region compared with pure anatase  $\text{TiO}_2$ .

For a high-quality single phase of products, the crystalline phases of nanotubes can be examined by X-ray diffraction (XRD). Figure 3 shows that all diffraction peaks of the metal-incorporated nanotubes (curves d and e) are similar with pure titanate nanotubes (curve c), and the structural framework is the same as

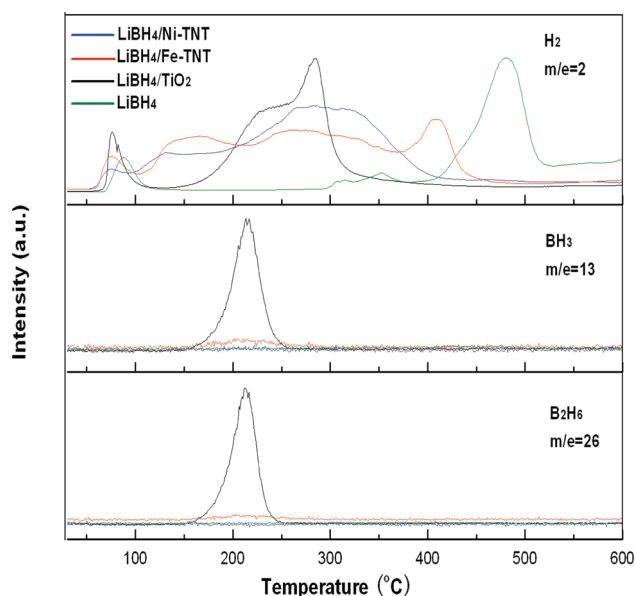


**Figure 4.** MS results of  $\text{LiBH}_4$ ,  $\text{LiBH}_4/\text{TiO}_2$  (anatase), and  $\text{LiBH}_4/\text{Ni(Fe)-TNT}$  between 30 and  $600^\circ\text{C}$  at a heating rate of  $5^\circ\text{C min}^{-1}$ .

that of  $\text{H}_2\text{Ti}_3\text{O}_7$  nanotubes<sup>26</sup> which is different from that of the precursor (curve a) and anatase titanate nanotubes (curve b). The curves indicate that the metal-incorporated nanotubes are high-purity single phased, and the structure can be indexed using  $\text{H}_2\text{Ti}_3\text{O}_7$  structure. The broadened diffraction peak is due to small crystal size.

**Hydrogen Release Performance.** Nonisothermal hydrogen evolutions for  $\text{LiBH}_4$  and  $\text{LiBH}_4/\text{TiO}_2$  (anatase, particle),  $\text{LiBH}_4/\text{Ni(Fe)-TNT}$  composites, ball milled 1.5 h at a rate of 350 rpm, are shown in Figure 4. The pristine  $\text{LiBH}_4$  sample starts to release significant  $\text{H}_2$  at about  $400^\circ\text{C}$ , and give broad desorption peak centered at  $450^\circ\text{C}$ . The hydrogen desorption is fully completed at  $550^\circ\text{C}$  with a total weight loss of 8.5% (Figure S2 of the Supporting Information), indicating that less than half of the hydrogen was released from the  $\text{LiBH}_4$ , in good agreement with the data in the literature.<sup>23</sup> The onset temperature of dehydrogenation for  $\text{LiBH}_4/\text{TiO}_2$  composite is around  $160^\circ\text{C}$  and with a maximal desorption peak between  $280$  and  $300^\circ\text{C}$ , and a shoulder at  $230$ – $250^\circ\text{C}$ . Unfortunately, the detrimental side products of  $\text{BH}_3$  and  $\text{B}_2\text{H}_6$  could be detected during the thermolysis. Compared with the neat  $\text{LiBH}_4$  and  $\text{LiBH}_4/\text{TiO}_2$  composite, the decompositions of  $\text{LiBH}_4/\text{Ni(Fe)-TNT}$  composites to release  $\text{H}_2$  occur below  $100^\circ\text{C}$  and end at about  $400^\circ\text{C}$ . Neither  $\text{BH}_3$  nor  $\text{B}_2\text{H}_6$  was detected during the decomposition. This is encouraging as these species are poisoning for fuel cells, although they are normally associated with the decomposition of transition metal borohydrides. From above results we can conclude that the decomposition mechanism of  $\text{LiBH}_4/\text{Ni(Fe)-TNT}$  composites is different from that of  $\text{LiBH}_4/\text{TiO}_2$ . Here, we propose that different nanotube structures between anatase and  $\text{H}_2\text{Ti}_3\text{O}_7$  induced the distinct decomposition products. To confirm the hypothesis, other two samples were synthesized:  $\text{LiBH}_4/\text{TNT}$  (anatase) and  $\text{LiBH}_4/\text{TNT}(\text{H}_2\text{Ti}_3\text{O}_7)$ . The thermolysis behaviors of samples are shown in Figure 5. It is noteworthy that neither  $\text{BH}_3$  nor  $\text{B}_2\text{H}_6$  was observed during decomposition of  $\text{LiBH}_4/\text{TNT}(\text{H}_2\text{Ti}_3\text{O}_7)$ , whereas they were detected in  $\text{LiBH}_4/\text{TNT}(\text{anatase})$  decomposition. This demonstrates that  $\text{H}_2\text{Ti}_3\text{O}_7$  can inhibit the formation of  $\text{BH}_3$  and  $\text{B}_2\text{H}_6$ , and a detailed discussion



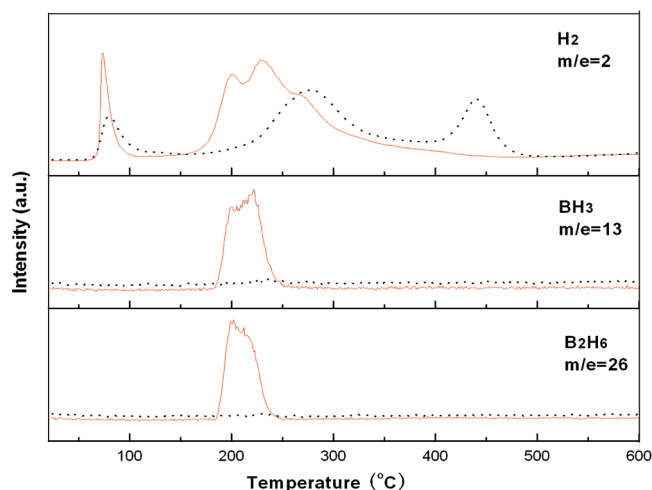


**Figure 5.** MS results of  $\text{LiBH}_4/\text{TNT}-(\text{anatase})$  (solid, red) and  $\text{LiBH}_4/\text{TNT}(\text{H}_2\text{Ti}_3\text{O}_7)$  (dot, black) between 30 and 600 °C at a heating rate of 5 °C  $\text{min}^{-1}$ .

is given at the end of the article. Recent researches indicate that Ni is an excellent catalyst for decomposition of complex hydride.<sup>12,30</sup> Note that the onset temperature of dehydrogenation for  $\text{LiBH}_4/\text{TNT}(\text{H}_2\text{Ti}_3\text{O}_7)$  in Figure 5 is 100 °C, higher than that of  $\text{LiBH}_4/\text{Ni}(\text{Fe})-\text{TNT}$  composites, suggesting that Ni and Fe are good catalysts to decrease the decomposition temperature of  $\text{LiBH}_4$ . Hydrogen evolution and weight loss for  $\text{LiBH}_4/\text{Ni}-\text{TNT}$ ,  $\text{LiBH}_4/\text{NiO}/\text{TNT}$  (ball-milled  $\text{LiBH}_4$  with NiO and  $\text{H}_2\text{Ti}_3\text{O}_7$  nanotubes) and  $\text{LiBH}_4/\text{Ni}/\text{TNT}$  (ball-milled  $\text{LiBH}_4$  with Ni and  $\text{H}_2\text{Ti}_3\text{O}_7$  nanotubes) are shown in Figure 6. Two hydrogen evolutions at 265 and 430 °C, were observed for  $\text{LiBH}_4/\text{NiO}/\text{TNT}$  with a total weight loss of 14 wt %. The dehydrogenation behavior of  $\text{LiBH}_4/\text{Ni}/\text{TNT}$  sample is similar to that of  $\text{LiBH}_4/\text{NiO}/\text{TNT}$ . In the case of  $\text{LiBH}_4/\text{Ni}-\text{TNT}$  sample, hydrogen released at lower temperature and at a much faster rate. This result may be caused by two facts. First, nickel is in better dispersion in  $\text{Ni}-\text{TNT}$  compared to  $\text{Ni}/\text{TNT}$  system. It was found that<sup>26</sup> in metal-incorporated nanotubes, metal atoms are monatomic dispersion located at the interlayer region of  $\text{H}_2\text{Ti}_3\text{O}_7$ , whereas it is difficult to do this by ball milling Ni and NiO. Second, it is due to different local coordination and environment of nickel atom. In metal-incorporated nanotubes, metal atoms are connected titanium through an oxygen bridge but, in ball-milled  $\text{LiBH}_4/\text{NiO}/\text{TNT}$  and  $\text{LiBH}_4/\text{Ni}/\text{TNT}$  samples, nickel and titanium are separated, and the synergistic catalytic effects of nickel and titanium seem to be very weak.

In Figure 7, isothermal hydrogen desorption profiles are utilized to compare the kinetic properties of  $\text{LiBH}_4/\text{Ni}(\text{Fe})-\text{TNT}$ ,  $\text{LiBH}_4/\text{TiO}_2$  composites and bulk  $\text{LiBH}_4$  samples. The hydrogen desorption rates are significantly higher for the  $\text{LiBH}_4/\text{Ni}(\text{Fe})-\text{TNT}$  samples as compared to  $\text{LiBH}_4/\text{TiO}_2$  and bulk  $\text{LiBH}_4$  samples at 120 °C, in particular, during the first 5000 s of measurements. It is noteworthy that  $\text{LiBH}_4$  in  $\text{LiBH}_4/\text{Fe}-\text{TNT}$  composite releases ~4.7 wt % hydrogen at a very low temperature 120 °C, whereas there is nearly no hydrogen released from the bulk  $\text{LiBH}_4$ . For  $\text{LiBH}_4/\text{TiO}_2$  sample, about 3 wt % hydrogen released from  $\text{LiBH}_4$  within 12 000 s, even prolonging the hydrogen desorption time to 32 000 s and the corresponding dehydrogenation capacity is only 3.6 wt %. However, it was found that the hydrogen released from  $\text{LiBH}_4$  in  $\text{LiBH}_4/\text{Ni}-\text{TNT}$  sample is only 2.5 wt %, the decrease in dehydrogen capacity due to decomposition during the ball-milling process. This is illustrated in Figure 8,

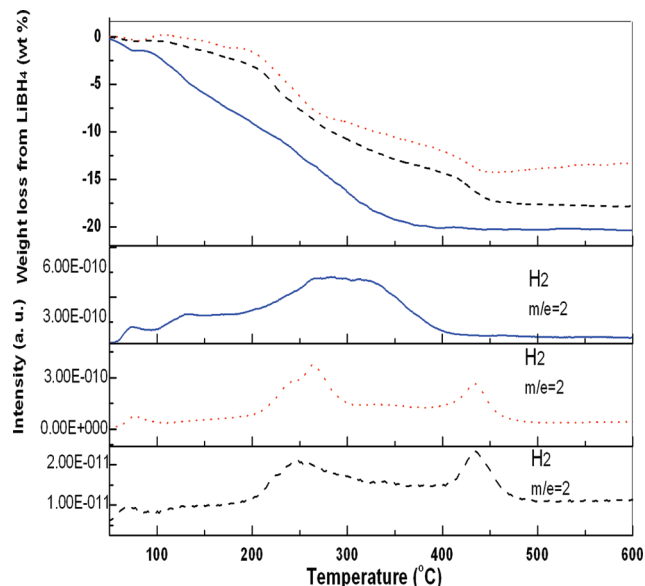


**Figure 6.** TGA (up) and MS (bottom) results for  $\text{LiBH}_4/\text{Ni}-\text{TNT}-$  (solid, blue),  $\text{LiBH}_4/\text{NiO}/\text{TNT}$  mixture (dot, red), and  $\text{LiBH}_4/\text{Ni}/\text{TNT}$  (dash, black).

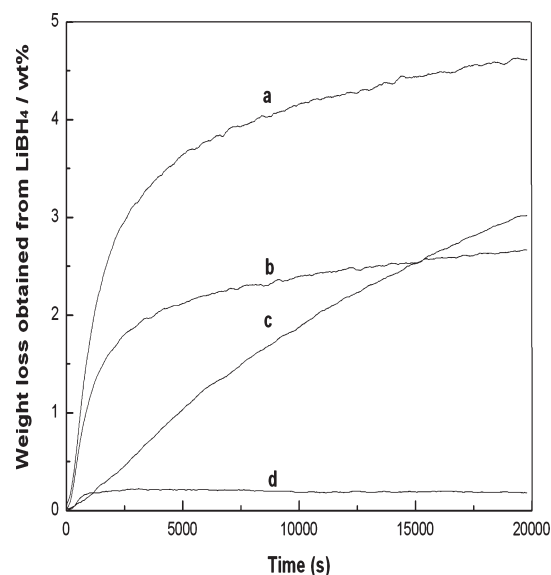


**Figure 7.** Hydrogen release from (a)  $\text{LiBH}_4/\text{Fe}-\text{TNT}$ , (b)  $\text{LiBH}_4/\text{Ni}-\text{TNT}$ , (c)  $\text{LiBH}_4/\text{TiO}_2$  composites, and (d) bulk  $\text{LiBH}_4$  at 120 °C.

the decrease in dehydrogen capacity due to decomposition during the ball-milling process. This is illustrated in Figure 8, which displays the isothermal dehydrogenation results for a 0.5 h (300 rpm) ball-milled  $\text{LiBH}_4/\text{Ni}-\text{TNT}(2)$  sample. It is encouraging to see that 4.5 wt % hydrogen liberated from  $\text{LiBH}_4$  at 120 °C and 11 wt % hydrogen liberated at 260 °C within 12 000 s. The phases present in the starting materials and dehydrogenation products were investigated by XRD, shown in Figure 9. The XRD pattern for the as-prepared  $\text{LiBH}_4/\text{Ni}-\text{TNT}(2)$  sample was found to consist of weak diffuse patterns for both the  $\text{H}_2\text{Ti}_3\text{O}_7$  and  $\text{LiBH}_4$  phases. After dehydrogenation at 120 °C, patterns of  $\text{H}_2\text{Ti}_3\text{O}_7$  disappeared and the phase of  $\text{Li}_x\text{TiO}_y$  are formed. The patterns of  $\text{Li}_x\text{TiO}_y$  become stronger as the dehydrogenation

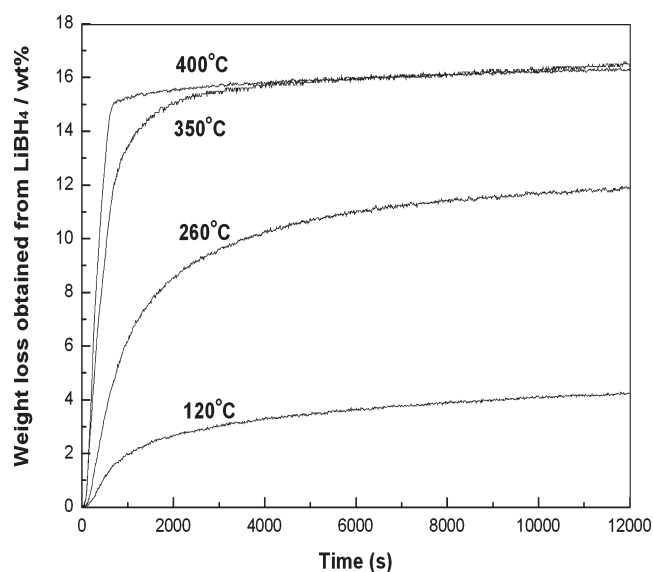


Figure 8. Isothermal hydrogen desorption profiles of  $\text{LiBH}_4/\text{Ni-TNT}(2)$  sample at different temperatures.

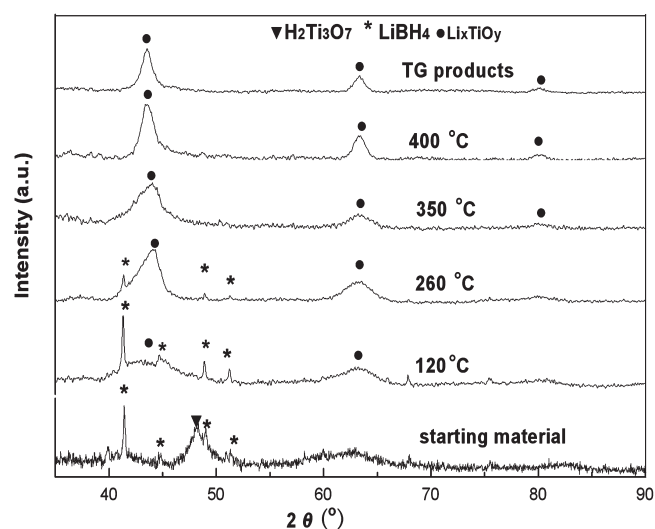


Figure 9. XRD patterns for  $\text{LiBH}_4/\text{Ni-TNT}(2)$  sample dehydrogenated at different temperatures.

temperature increases. In XRD measurements no Ni species are detected, due to its low content. After heating to 600 °C (5 °C/min), the XRD pattern for the TG products corresponded to  $\text{Li}_x\text{TiO}_y$  ( $\text{LiTiO}_2$ ). The fact that no boron-containing phases were identified by analysis of the XRD patterns in Figure 9 suggests that the boron-containing phases were in an amorphous state.

Attempts to directly rehydride the decomposition product by heating at 400 °C and 4 MPa  $\text{H}_2$  pressure have not achieved significant hydrogenation; hence an alternative hydrogenation route would be required to reform the  $\text{LiBH}_4$ . The morphology of as-prepared  $\text{LiBH}_4/\text{Ni-TNT}(2)$  sample and dehydrogenation products of different temperatures are shown in Figure 10. SEM image of  $\text{LiBH}_4/\text{Ni-TNT}(2)$  sample shows that the composite is composed of many coarse particles, which is different from the morphology of nanotubes shown in part d of Figure 1.

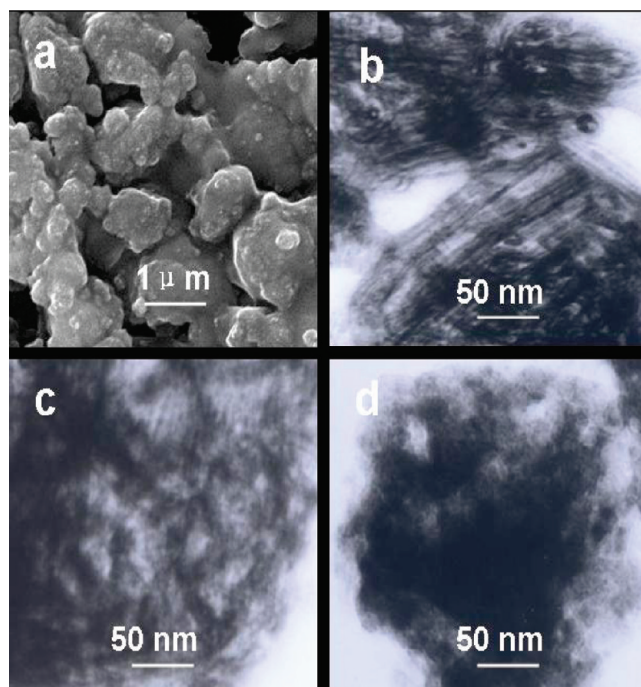
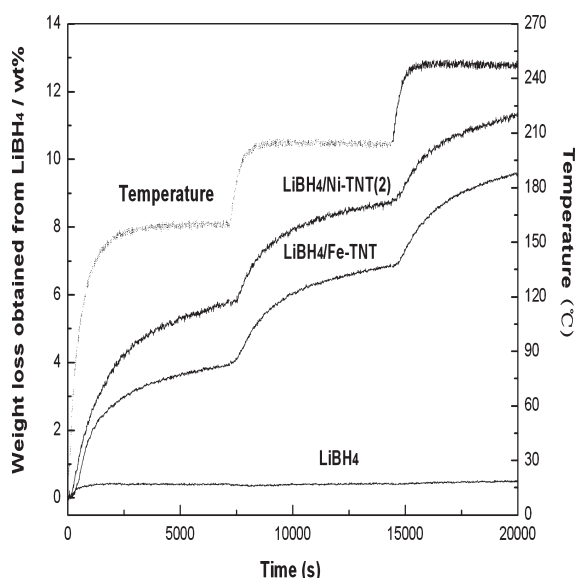


Figure 10. (a) SEM image of  $\text{LiBH}_4/\text{Ni-TNT}(2)$  sample; (b) TEM image of  $\text{LiBH}_4/\text{Ni-TNT}(2)$  sample; (c) TEM image of  $\text{LiBH}_4/\text{Ni-TNT}(2)$  sample dehydrogenated at 260 °C. (d) TEM image of  $\text{LiBH}_4/\text{Ni-TNT}(2)$  sample dehydrogenated at 400 °C.

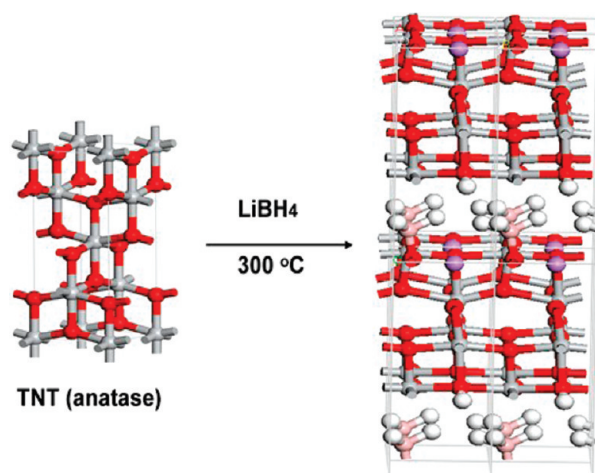
From the TEM image of  $\text{LiBH}_4/\text{Ni-TNT}(2)$  sample (part b of Figure 9) nanotubes can be easily identified, indicating that the ball-milling process induced the aggregation between  $\text{LiBH}_4$  and nanotubes, but did not destroy the tubular structure of nanotubes. As increasing the dehydrogenation temperature, tubular structure disappeared gradually. We can conclude that lithium insertion into  $\text{H}_2\text{Ti}_3\text{O}_7$  structure induced the destruction of nanotubes. This result also suggests that  $\text{H}_2\text{Ti}_3\text{O}_7$  nanotubes may be not suitable electrode material for Li ion batteries.

Figure 11 displays the hydrogen desorption curves for  $\text{LiBH}_4/\text{Ni-TNT}(2)$ ,  $\text{LiBH}_4/\text{Fe-TNT}$  and bulk  $\text{LiBH}_4$  samples. During the whole temperature region,  $\text{LiBH}_4/\text{Ni-TNT}(2)$  and  $\text{LiBH}_4/\text{Fe-TNT}$  samples have similar dehydrogenation behaviors and the released hydrogen content is higher for  $\text{LiBH}_4/\text{Ni-TNT}(2)$ . It is about 60% of the hydrogen content released from  $\text{LiBH}_4/\text{Ni-TNT}(2)$  sample at  $T \leq 220$  °C. In contrast, nearly no hydrogen released from the bulk  $\text{LiBH}_4$ .

**Interaction between  $\text{LiBH}_4$  and Nanotubes.** Figure 5 shows that the onset decomposition temperature of  $\text{LiBH}_4/\text{TNT}(\text{anatase})$  is lower than that of  $\text{LiBH}_4/\text{TNT}(\text{H}_2\text{Ti}_3\text{O}_7)$ . Figure 5 also presents that the detrimental side products of borane and diborane could be detected during the  $\text{LiBH}_4/\text{TNT}(\text{anatase})$  thermolysis, whereas they were not observed for  $\text{LiBH}_4/\text{TNT}(\text{H}_2\text{Ti}_3\text{O}_7)$  sample. To get an insight to these phenomena, we performed the first-principle calculations to investigate the interaction mechanism between  $\text{LiBH}_4$  and nanotubes. Figure 12 shows reaction between  $\text{TNT}(\text{anatase})$  and  $\text{LiBH}_4$  at 300 °C. In  $\text{TNT}(\text{anatase})$  nanotube structure, every oxygen atom links to three titanium atoms, and all oxygen atoms are in the same chemical environment. During the thermal decomposition, one hydrogen atom from  $\text{LiBH}_4$  first transferred to oxygen atom, then Li atom was attracted and captured by five oxygen atoms rather than titanium



**Figure 11.** Time dependence of hydrogen desorption from  $\text{LiBH}_4/\text{Ni-TNT}(2)$ ,  $\text{LiBH}_4/\text{Fe-TNT}$ , and bulk  $\text{LiBH}_4$  samples.



**Figure 12.** Reaction between anatase nanotube with  $\text{LiBH}_4$  (Ti, gray; O, red; B, pink; Li, purple; H, white.).

atoms, and leaving  $\text{BH}_3$  group combined with O atom. Figure 13 shows the dynamics behaviors between  $\text{TNT}(\text{H}_2\text{Ti}_3\text{O}_7)$  and  $\text{LiBH}_4$  at  $300^\circ\text{C}$ . Left picture is the crystal structure of two unit cells of  $\text{H}_2\text{Ti}_3\text{O}_7$ , that is a structural unit of  $\text{H}_4\text{Ti}_6\text{O}_{14}$ . Oxygen atoms occupy four different kinds of sites in the lattice. During the dynamics process, Li atom was separated from the  $\text{LiBH}_4$  molecular first, leaving  $\text{BH}_4^-$  combined with the four  $-\text{OH}$  groups of  $\text{H}_2\text{Ti}_3\text{O}_7$  and rotated throughout the whole simulation but did not decomposition. Because interaction of  $\text{B}-\text{H}^{\delta-} \cdots \delta^+ \text{H}-\text{O}$  stabilized the  $\text{BH}_4^-$  and restricted its decomposition, so the onset decomposition temperature for hydrogen release of  $\text{LiBH}_4/\text{TNT}(\text{H}_2\text{Ti}_3\text{O}_7)$  is higher than that of  $\text{LiBH}_4/\text{TNT}(\text{anatase})$ . However, this simulation results can not explain clearly why  $\text{BH}_3$  and  $\text{B}_2\text{H}_6$  are generated in  $\text{LiBH}_4/\text{TNT}(\text{anatase})$ . Generally, the release of  $\text{BH}_3$  and  $\text{B}_2\text{H}_6$  implying that the interaction between  $\text{TNT}(\text{anatase})$  and  $\text{BH}_3$  is weak, while the interaction between  $\text{TNT}(\text{H}_2\text{Ti}_3\text{O}_7)$  and  $\text{BH}_3$  is strong. Following this idea, we calculated the interactions between  $\text{BH}_3$

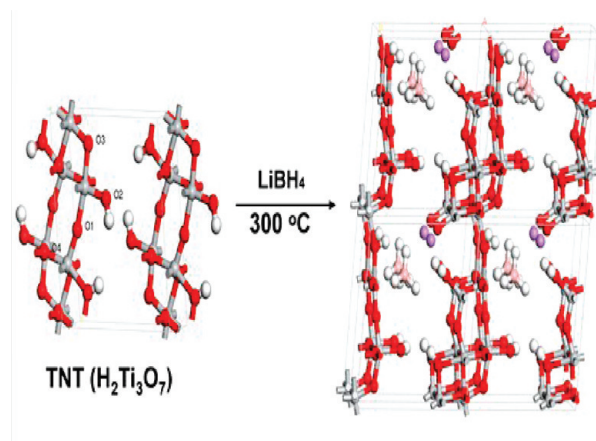


**Figure 13.** Reaction between  $\text{H}_2\text{Ti}_3\text{O}_7$  nanotube with  $\text{LiBH}_4$  (Ti, gray; O, red; B, pink; Li, purple; H, white.).

and these two types of TNT and found that  $\text{BH}_3$  prefers to combine with oxygen atoms at O3 position in the  $\text{H}_2\text{Ti}_3\text{O}_7$  structure (Figure 13), the length of  $\text{B}-\text{O}$  bond is  $1.49 \text{ \AA}$  and the adsorption energy is  $-1.40 \text{ eV}$  (the negative adsorption energy means the  $\text{BH}_3$  can be adsorbed). While in the anatase structure, the bond length of  $\text{B}-\text{O}$  is  $1.53 \text{ \AA}$  and the adsorption energy is  $0.76 \text{ eV}$  (the positive adsorption energy means the  $\text{BH}_3$  can not be adsorbed). The stronger interaction between  $\text{BH}_3$  and  $\text{H}_2\text{Ti}_3\text{O}_7$  indicates that  $\text{H}_2\text{Ti}_3\text{O}_7$  structure is better for stabilization of boracic impurities.

## CONCLUSIONS

In an attempt to destabilize lithium borohydride, metal-incorporated titanate nanotubes have been selected and evaluated as possible destabilization agents. The experimental results show that ball milling  $\text{LiBH}_4$  with metal-incorporated titanate nanotubes reduced the onset temperature for dehydrogenation to  $100^\circ\text{C}$ . Destabilization of the borohydride was through metal catalysis and reaction with  $\text{H}_2\text{Ti}_3\text{O}_7$  nanotubes forming  $\text{LiTiO}_2$ . For  $\text{LiBH}_4/\text{Ni-TNT}(2)$  sample,  $4.5 \text{ wt } \%$  hydrogen liberated from  $\text{LiBH}_4$  at  $120^\circ\text{C}$ , and  $11 \text{ wt } \%$  hydrogen liberated at  $260^\circ\text{C}$  within 200 min. We also found that different structures of nanotubes caused different decomposition mechanisms, for  $\text{LiBH}_4$  and  $\text{H}_2\text{Ti}_3\text{O}_7$  composites the generation of boracic impurities could be efficiently prohibited during their decomposition.

## ASSOCIATED CONTENT

**Supporting Information.** UV-vis absorption spectra and TG curves of decomposition reactions. This material is available free of charge via the Internet at <http://pubs.acs.org>.

## AUTHOR INFORMATION

### Corresponding Author

\*Tel./Fax: +86-411-84379213. E-mail: [lxsun@dicp.ac.cn](mailto:lxsun@dicp.ac.cn) (L.S.); [xufen@lnnu.edu.cn](mailto:xufen@lnnu.edu.cn) (F.X.). Email: [tliuyl@jnu.edu.cn](mailto:tliuyl@jnu.edu.cn) (L.Y.).

## ACKNOWLEDGMENT

The authors wish to acknowledge the financial support from the National Basic Research Program (973 program) of China (2010CB631303), the National Natural Science Foundation of



China (Nos. 20833009, 20873148, 20903095, 50901070, 51071146, 51071081, and U0734005), IUPAC (Project No. 2008-006-3-100), the Joint Project of Guangdong Province and Chinese Academy of Sciences (2010A090100034), Dalian Scientific Project (2009A11GX052), and the State Key Laboratory of Explosion Science and Technology, Beijing Institute of Technology (Grant No. KFJJ10-1Z).

## REFERENCES

- (1) Bogdanovic, B.; Schwickardi, M. *J. Alloys Compd.* **1997**, *253*, 1–9.
- (2) Chen, P.; Xiong, Z. T.; Luo, J. Z.; Lin, J. Y.; Tan, K. L. *Nature* **2002**, *420*, 302–304.
- (3) Grochala, W.; Edwards, P. P. *Chem. Rev.* **2004**, *104*, 1283–1315.
- (4) Schlapbach, L.; Züttel, A. *Nature* **2001**, *414*, 353–358.
- (5) Schuth, F.; Bogdanovic, B.; Felderhoff, M. *Chem. Commun.* **2004**, 2249–2258.
- (6) Bogdanovic, B.; Ritter, A.; Spliethoff, B. *Angew. Chem., Int. Ed.* **1990**, *29*, 223–234.
- (7) Chen, J.; Kuriyama, N.; Xu, Q.; Takeshita, H. T.; Sakai, T. *J. Phys. Chem. B* **2001**, *105*, 11214–11220.
- (8) Züttel, A.; Wenger, P.; Rentsch, S.; Sudan, P.; Mauron, P.; Emmenegger, C. *J. Power Sources* **2003**, *118*, 1–7.
- (9) Züttel, A.; Rentsch, S.; Fischer, P.; Wenger, P.; Sudan, P.; Mauron, P.; Emmenegger, C. *J. Alloys Compd.* **2003**, *356*, S15–S20.
- (10) Au, M.; Jurgensen, A. *J. Phys. Chem. B* **2006**, *110*, 7062–7067.
- (11) Au, M.; Jurgensen, A.; Zeigler, K. *J. Phys. Chem. B* **2006**, *110*, 26482–26487.
- (12) Varin, R. A.; Zbronic, L. *Int. J. Hydrogen Energy* **2010**, *35*, 3588–3597.
- (13) Zhang, B. J.; Liu, B. H. *Int. J. Hydrogen Energy* **2010**, *35*, 7288–7294.
- (14) Meisner, G. P.; Scullin, M. L.; Balogh, M. P.; Pinkerton, F. E.; Meyer, M. S. *J. Phys. Chem. B* **2006**, *110*, 4186–4192.
- (15) Crosby, K.; Shaw, L. L. *Int. J. Hydrogen Energy* **2010**, *35*, 7519–7529.
- (16) Price, T. E. C.; Grant, D. M.; Legrand, V.; Walker, G. S. *Int. J. Hydrogen Energy* **2010**, *35*, 4154–4161.
- (17) Fan, M. Q.; Sun, L. X.; Zhang, Y.; Xu, F.; Zhang, J.; Chu, H. L. *Int. J. Hydrogen Energy* **2008**, *33*, 74–80.
- (18) Zhang, Y.; Zhang, W. S.; Wang, A. Q.; Sun, L. X.; Fan, M. Q.; Chu, H. L.; Sun, J. C.; Zhang, T. *Int. J. Hydrogen Energy* **2007**, *32*, 3976–3980.
- (19) Gross, A. F.; Vajo, J. J.; Van Atta, S. L.; Olson, G. L. *J. Phys. Chem. C* **2008**, *112*, S651–S657.
- (20) Vajo, J. J.; Skeith, S. L.; Mertens, F. *J. Phys. Chem. B* **2005**, *109*, 3719–3722.
- (21) Yu, X. B.; Grant, D. M.; Walker, G. S. *Chem. Commun.* **2006**, 3906–3908.
- (22) Pinkerton, F. E.; Meisner, G. P.; Meyer, M. S.; Balogh, M. P.; Kundrat, M. D. *J. Phys. Chem. B* **2005**, *109*, 6–8.
- (23) Yu, X. B.; Grant, D. A.; Walker, G. S. *J. Phys. Chem. C* **2008**, *112*, 11059–11062.
- (24) Brun, N.; Janot, R.; Sanchez, C.; Deleuze, H.; Gervais, C.; Morcrette, M.; Backov, R. *Energy Environ. Sci.* **2010**, *3*, 824–830.
- (25) Bavykin, D. V.; Lapkin, A. A.; Plucinski, P. K.; Friedrich, J. M.; Walsh, F. C. *J. Phys. Chem. B* **2005**, *109*, 19422–19427.
- (26) Ding, X.; Xu, X. G.; Chen, Q.; Peng, L. M. *Nanotechnology* **2006**, *17*, S423–S427.
- (27) Payne, M. C.; Teter, M. P.; Allan, D. C.; Arias, T. A.; Joannopoulos, J. D. *Rev. Mod. Phys.* **1992**, *64*, 1045–1097.
- (28) Perdew, J. P.; Burke, K.; Ernzerhof, M. *Phys. Rev. Lett.* **1996**, *77*, 3865–3868.
- (29) Vanderbilt, D. *Phys. Rev. B* **1990**, *41*, 7892–7895.
- (30) Choudhury, P.; Srinivasan, S. S.; Bhethanabotla, V. R.; Goswami, Y.; McGrath, K.; Stefanakos, E. K. *Int. J. Hydrogen Energy* **2009**, *34*, 6325–6334.